Uniform-load and actuator influence functions of a thin or thick annular mirror: application to active mirror support optimization

Luc Arnold

Explicit analytical expressions are derived for the elastic deformation of a thin or thick mirror of uniform thickness and with a central hole. Thin-plate theory is used to derive the general influence function, caused by uniform and/or discrete loads, for a mirror supported by discrete points. No symmetry considerations of the locations of the points constrain the model. An estimate of the effect of the shear forces is added to the previous pure bending model to take into account the effect of the mirror thickness. Two particular cases of general influence are considered: the actuator influence function and the uniform-load (equivalent to gravity in the case of a thin mirror) influence function for a ring support of k discrete points with k-fold symmetry. The influence of the size of the support pads is studied. A method for optimizing an active mirror cell is presented that couples the minimization of the gravity influence function with the optimization of the combined actuator influence functions to fit low-order aberrations. These low-spatial-frequency aberrations can be of elastic or optical origin. In the latter case they are due, for example, to great residual polishing errors corresponding to the soft polishing specifications relaxed for cost reductions. Results show that the correction range of the active cell can thus be noticeably enlarged, compared with an active cell designed as a passive cell, i.e., by minimizing only the deflection under gravitational loading. In the example treated here of the European Southern Observatory's New Technology Telescope I show that the active correction range can be enlarged by ~50% in the case of third-order astigmatic correction.

Key words: Telescope mirrors, mirror deformations, elasticity, mirror supports, passive supports, active optics, optimization.

1. Introduction

The primary-mirror deformation of telescopes, because of gravitational or actuator loadings, is often studied by computer-intensive finite element analysis (FEA). In some cases these deformations can also be described in analytical form. This permits a rapid estimate of mirror deformation, which is convenient for active or passive-support optimization iterative processes. The deformation under uniform loading, the so-called uniform-load influence function (ULIF), of a circular thin mirror was studied by Couder[1] using the thin-plate bending theory.[2,3] He gave an analytical expression for the pure bending deformation on a continuous ring support as well as the well-known scaling law that relates deformation to mirror diameter and thickness, either for continuous or discrete supports. Nelson *et al.*[4] gave an analytical form to the ULIF of a thin mirror without a central hole and supported on a ring of k discrete points of k-fold symmetry. The deformation under uniform gravitational loading, the so-called gravity influence function (GIF), and the ULIF are identical when computed by the thin-plate theory. For a thick mirror the ULIF and the GIF are slightly different.[5] Selke[6] and Schwesinger[7] gave exact expressions for the ULIF and the GIF, respectively. However, they limited their studies to a continuous ring support of negligible width. Schwesinger[8] also presented a method to extend the GIF to a ring of k discrete points having k-fold symmetry. Wan *et al.*[9] proposed a general analytical method, adapted from Ref. 3, to estimate the extra deflection caused by

When this research was performed, the author was with the Laboratoire d'Astrophysique Observationelle, Collège de France et Observatoire de la Côte d'Azur, 2130 route de l'Observatoire, 06460 Caussols, France. The author is now with the Laboratoire d'Astrophysique Observationelle, Collège de France, Observatoire de Haute Provence 04 870, Saint-Michel-l'Observatoire, France.e-mail may be addressed to arnold@obs-hp.fr.

Received 25 January 1995; revised manuscript received 31 July 1995.

0003-6935/96/071095-12$06.00/0

shear forces directly from a thin-plate model. Menikoff[10] derived from thin-plate theory the deformation from a concentrated force, the so-called actuator influence function (AIF). Several other solutions for thin plates and different kinds of loading and edge conditions can be found in Ref. 3.

In this paper I extend these previous studies by giving explicit analytical expressions for the deflection of a thin or thick mirror of uniform thickness with a central hole and supported by discrete points. No symmetry consideration of the support topology constrains the model. Uniform (ULIF) and discrete (AIF) loadings are considered in Section 3. The series for estimating shear effects is also included. In Section 4 two particular force distributions are considered, the pure AIF and the ULIF derived for a ring support of k points with k-fold symmetry. The influence of the support pads' size is discussed in Section 5.

A mirror support, either passive or active, must typically minimize the variance of the mirror's residual deflection (but the slopes are also relevant for image degradation in the atmosphere,[11] and so a trade-off can be found). As suggested by Ostroff[12] and Ray and Chung[13] this is equivalent to minimizing the actuators' input on high-order bending modes that cannot be controlled efficiently by active support. A method of optimization of an active primary-mirror cell is proposed in Section 6. With the method the GIF coupled with the optimization of combinations of AIF's fitting low-order aberrations, such as astigmatism, is minimized. It is shown that the correcting range of an active cell can thus be noticeably enlarged if an approach specific to active (as opposed to passive) cells is used from the outset.

2. Notation

r, θ, polar coordinates;
w, deflection;
w_s, deflection caused by shear forces;
a, mirror's outer radius;
b, support radius from the mirror center;
c, mirror's inner radius (central-hole radius);
ρ_0, normalized mirror inner radius ($\rho_0 = c/a$);
h, mirror thickness;
q, load per unit area applied to the mirror;
P, f, forces applied to the mirror;
E, Young's modulus;
ν, Poisson's ratio;
$D = Eh^3/[12(1 - \nu^2)]$ = flexure rigidity;
$G = E/[2(1 + \nu)]$ = shear rigidity;
$\nabla^2 = \partial^2/\partial r^2 + 1/r(\partial/\partial r) + 1/r^2(\partial^2/\partial\theta^2)$ = Laplacian operator.

Figure 1 shows the mirror model according to this notation. Note that P typically represents the mirror weight or the resultant force of uniform pressure integrated over the mirror surface.

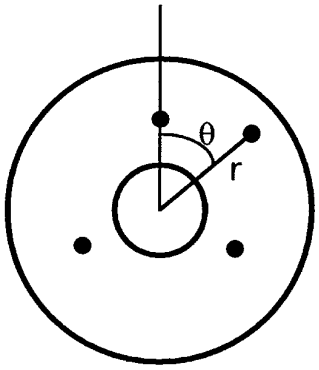

Fig. 1. Top view of a mirror with a central hole. In this example, four discrete axial forces are applied to the mirror. Three of them are arranged with threefold symmetry.

3. General Form of the Influence Functions

A circular horizontal thin mirror with a central hole is considered. It is in static equilibrium with force P, resulting from uniform loading (typically its weight), and a set of k concentrated forces (Fig. 1), each provided by a discrete support point on the rear mirror's surface. Each support j is characterized by its forces f_j and its polar coordinates b_j and θ_j. The origin of the coordinates is the mirror center. The thin-plate bending theory[3] leads to

$$D\nabla^2(\nabla^2 w) = q \tag{1}$$

from which deformation w, normal to the mirror's middle surface, must be derived. Load q is given by

$$q(r, \theta) = q = \frac{-P}{\pi(a^2 - c^2)} + \sum_{j=1}^{k} \frac{f_j}{b_j}\delta(r - b_j)\delta(\theta - \theta_j) \tag{2}$$

or

$$q(r, \theta) = q = \frac{-P}{\pi(a^2 - c^2)} + \sum_{j=1}^{k} \frac{f_j}{2\pi b_j} \times \delta(r - b_j) \sum_{m=-\infty}^{\infty} \exp[im(\theta - \theta_j)], \tag{3}$$

where the Dirac function $\delta(\theta - \theta_j)$ has been replaced by its complex Fourier series. Here it is thus assumed that the diameter of the support pad is negligible with respect to a. The static equilibrium states that the sums of applied forces and moments are zero, i.e.,

$$\sum_{j=1}^{k} f_j - P = 0, \tag{4}$$

$$\sum_{j=1}^{k} f_j b_j \exp(i\theta_j) = 0, \tag{5}$$

respectively. The mirror is assumed to satisfy the condition of the free-edge boundaries. Therefore

$$M_r(a) = M_r(c) = 0, \tag{6}$$

$$Q_r(a) - \frac{1}{r}\frac{\partial M_{r\theta}(a)}{\partial \theta} = Q_r(c) - \frac{1}{r}\frac{\partial M_{r\theta}(c)}{\partial \theta} = 0, \tag{7}$$

where M_r is the radial bending moment, Q_r is the resultant radial force perpendicular to the mirror's middle surface, and $M_{r\theta}$ is the twisting moment. The expressions for M_r, Q_r, and $M_{r\theta}$ versus w can be found in Ref. 3, 4, or 10. A classic method of solving Eq. (1), with Eqs. (6) and (7), consists of seeking a complex Fourier series of the form[3,4,10]

$$w(r, \theta) = \sum_{m=-\infty}^{\infty} w_m(r)\exp(im\theta). \tag{8}$$

Thus Eq. (1) becomes for the harmonic $m = 0$

$$\left(\frac{\partial^2}{\partial r^2} + \frac{1}{r}\frac{\partial}{\partial r}\right)^2 w_0 = \frac{-P}{\pi(a^2 - c^2)D} + \sum_{j=1}^{k} \frac{f_j}{2\pi b_j D}\,\delta(r - b_j). \tag{9}$$

Because

$$\sum_{j=1}^{k} f_j - P = 0, \tag{4}$$

Eq. (9) can be written as

$$\left(\frac{\partial^2}{\partial r^2} + \frac{1}{r}\frac{\partial}{\partial r}\right)^2 w_0 = \sum_{j=1}^{k} \frac{f_j}{\pi D}\left[\frac{-1}{a^2 - c^2} + \frac{\delta(r - b_j)}{2b_j}\right]. \tag{10}$$

In Eq. (10) is described the deflection of a mirror supported on k concentric rings of radii b_j. The total deflection w_0 is similar to a superposition of k deflections w_{0j} describing the shape of a mirror of weight f_j, which can be of opposite sign of gravity, supported by ring b_j. For $m \neq 0$

$$\left(\frac{\partial^2}{\partial r^2} + \frac{1}{r}\frac{\partial}{\partial r} - \frac{m^2}{r^2}\right)^2 w_m = \sum_{j=1}^{k} \frac{f_j}{2\pi b_j D}\exp(-im\theta_j)\delta(r - b_j). \tag{11}$$

At $r = b_j$ deformation w_m must satisfy the following three continuity conditions:

$$\lim_{r\to b_j^+} w_m = \lim_{r\to b_j^-} w_m, \tag{12}$$

$$\lim_{r\to b_j^+} \frac{\partial w_m}{\partial r} = \lim_{r\to b_j^-} \frac{\partial w_m}{\partial r}, \tag{13}$$

$$\lim_{r\to b_j^+} \frac{\partial^2 w_m}{\partial r^2} = \lim_{r\to b_j^-} \frac{\partial^2 w_m}{\partial r^2}, \tag{14}$$

and a fourth jump condition, caused by the jump in the resultant radial force Q_r,

$$\lim_{r\to b_j^+} \frac{\partial^3 w_m}{\partial r^3} - \lim_{r\to b_j^-} \frac{\partial^3 w_m}{\partial r^3} = \frac{f_j}{2\pi b_j D}\exp(-im\theta_j). \tag{15}$$

The general solutions of the homogeneous equation associated with Eq. (11) are[3,10]

$$m = 0, \quad w_0(r) = A_0 + B_0 r^2 + C_0 \ln(r) + D_0 r^2 \ln(r), \tag{16}$$

$$m = 1, \quad w_1(r) = A_1 r + B_1 r^3 + C_1/r + D_1 r \ln(r), \tag{17}$$

$$m > 1, \quad w_m(r) = A_m r^m + B_m r^{m+2} + C_m r^{-m} + D_m r^{-m+2}, \tag{18}$$

where A, B, C, and D are constants defined over the annular surface of a mirror limited by rings $r = b_j$ and b_{j+1}. The k supports form $k + 1$ annular surfaces, and, for a given value of m, $4(k + 1)$ constants A, B, C, D must be determined. They are derived from the $4 \times k$ conditions at $r = b_j$ and the four edge conditions at $r = c$ and a. The zero-net force and zero-net moment equations [Eqs. (4) and (5), respectively] permit one to calculate forces f_j. The general solutions, given by Eqs. (16)–(18), inserted into the continuity and jump equations, Eqs. (12)–(15), respectively, give A, B, C, and D jumps, as noted by Menikoff,[10] $\Delta_j A, \ldots, \Delta_j D$, with

$$\Delta_j A = \lim_{r\to b_j^+} A - \lim_{r\to b_j^-} A. \tag{19}$$

Note the typographical errors in Ref. 10: For correct values the jumps in Eq. (22) must be multiplied by one-half and Eq. (23) must be written as

$$\Delta_j B_0 = \frac{-q_j}{8\pi D}(\ln b_j + 1).$$

The total deflection w is then obtained by adding to w_0 the real part $w_{m\geq 1}(r, \theta)$ according to

$$w_{m\geq 1}(r, \theta) = \mathrm{Re}[2 \times w_{m\geq 1}(r) \times \exp \mathrm{im}\,\theta], \tag{20}$$

where $w_{m\geq 1}(r)$ is a complex function of $A_{m\geq 1}$, $B_{m\geq 1}$, $C_{m\geq 1}$, $D_{m\geq 1}$, and r.

Wan *et al.*[9] have shown that the extra deflection induced by the shear forces, neglected in the thin-plate theory, can be directly estimated from the pure bending model according to

$$w_s = -\frac{3}{2h}\frac{D}{G}\nabla^2 w. \tag{21}$$

The terms of the Fourier series for w_s are thus proportional to the Laplacian of w given by

$$m = 0, \quad \nabla^2 w_0(r) = 4[B_0 + D_0[\ln(r) + 1]], \tag{22}$$

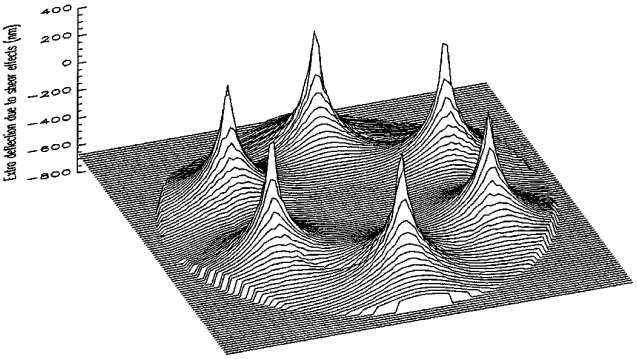

Fig. 2. Estimated extra deflection caused by shear forces, as computed for the ESO NTT 3.6-m primary mirror (Table 1) on a hypothetical six-point support with sixfold symmetry. This simple support, instead of the real 78-point one, was chosen for clarity.

$$m = 1, \quad \nabla^2 w_1(r) = 8B_1 r + 2D_1/r, \tag{23}$$

$$m > 1, \quad \nabla^2 w_m(r) = 4(m + 1)B_m r^m + 4(1 - m)D_m r^{-m}. \tag{24}$$

When w_s is added to w, the general influence function of a thick mirror with a central hole is fully characterized. Nevertheless w_s, as calculated with Eq. (21) with either the series giving w derived by Nelson *et al.*[4] or the series given in Section 4, shows a small artifact between the support points along radius b. Note that the artifact is also visible in Figs. 5 and 6 of Wan *et al.*[9] This is probably due to the approximation used in Wan's method. Figures 2 and 3 show the artifact when shear effects are computed for the primary mirror of the 3.6-m New Technology Telescope (NTT) of the European Southern Observatory (ESO) (Table 1). The artifact is visible along the supporting radius at $b = 1.2$ m. The apparent slope discontinuity at the support radius is typical of elastic deformation including shear effects[5–7]: w_s gives the average deflection across the thickness. But exact three-dimensional calculations[7] show that shear effects are dispersed across the thickness from the support to the optical surface. The surface is thus smoothed and has a smaller rms error.

Table 1. ESO NTT Primary Mirror and Support[a]

Parameters	Values (m)
Mirror outer radius a	1.7900
Mirror inner radius c	0.2826
Internal stop radius	0.5593
Support radii	
b_1 (8 pads, $\eta_1 = 0.10177$)	0.4544
b_2 (16 pads, $\eta_2 = 0.20491$)	0.8309
b_3 (24 pads, $\eta_3 = 0.31467$)	1.2263
b_4 (30 pads, $\eta_4 = 0.37865$)	1.6298
Pad radius	0.025
h	0.241
E	9.1×10^{10} Pa
ν	0.245

[a]Data are from the current design. The support radii have been optimized for the entire mirror surface, from the inner hole to the outer edge. The variable η_i represents a fraction of weight supported by ring i of radius b_i. Adapted from Ref. 7.

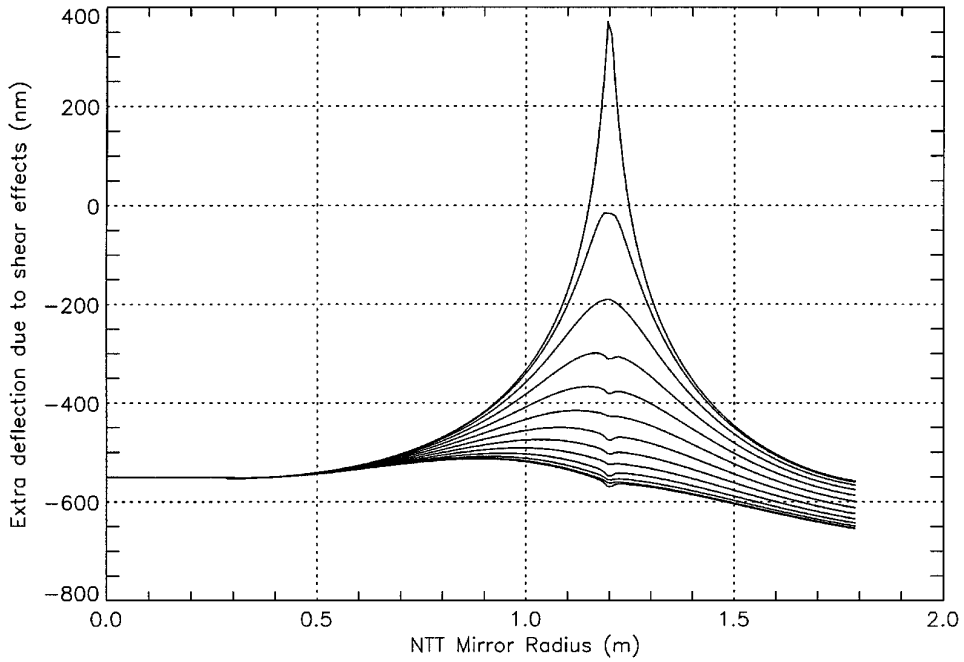

Fig. 3. Radial shear deflections, equally angularly spaced, for azimuth on the mirror going from a radius with a supporting point to a radius between two supporting points. The artifact along the supporting radius (1.2 m) is visible. The same six-point support as in Fig. 2 is shown.

4. Particular Forms of the Influence Functions

A. Pure Concentrated Forces

This case corresponds to $P = 0$. Equation (9), which describes the deformation for $m = 0$, then becomes

$$\left(\frac{\partial^2}{\partial r^2} + \frac{1}{r}\frac{\partial}{\partial r}\right)^2 w_0 = \sum_{j=1}^{k} \frac{f_j}{2\pi b_j D}\,\delta(r - b_j) \tag{25}$$

and is similar to Eq. (11) for $m \neq 0$. Menikoff[10] gives a method for building up coefficients A, B, C, and D. Because of the central hole, the expressions for constants B_0, C_0, B_1, and C_1 at the outer edge are

$$B_0 = \alpha_0 \frac{c^2}{c^2 - a^2}, \tag{26}$$

$$C_0 = 2\alpha_0\left(\frac{1 + \nu}{1 - \nu}\right)\frac{c^2 a^2}{c^2 - a^2}, \tag{27}$$

with

$$\alpha_0 = \sum_{j=1}^{k} \Delta_j B_0 - \frac{1}{2c^2}\left(\frac{1 - \nu}{1 + \nu}\right)\sum_{j=1}^{k} \Delta_j C_0, \tag{28}$$

$$B_1 = \alpha_1 \frac{c^4}{c^4 - a^4}, \tag{29}$$

$$C_1 = -\alpha_1\left(\frac{3 + \nu}{1 - \nu}\right)\frac{c^4 a^4}{c^4 - a^4}, \tag{30}$$

with

$$\alpha_1 = \sum_{j=1}^{k} \Delta_j B_1 + \frac{1}{c^4}\left(\frac{1 - \nu}{3 + \nu}\right)\sum_{j=1}^{k} \Delta_j C_1. \tag{31}$$

Because A_0, D_0, A_1, and D_1 cancel at the mirror's outer edge, the eight coefficients for $m = 0$ and $m = 1$ can be built up from the outer to the inner edges. For $m > 1$ the two boundary conditions at the inner edge must be transferred to the outer edge by jumps. Associated with the boundary conditions at the outer edge, a set of four equations to be solved for A_m, B_m, C_m, and D_m at $r = a$ is provided.

A word is necessary concerning calculation of a new set of k forces f_j after a given change in one force f_i on one actuator. If $k > 4$, the problem of mirror equilibrium becomes hyperstatic. The active mirror can be considered as a rigid body reacting on three hard points of the support and then deformed by a set of soft actuators, i.e., modeled by a soft spring, also fixed to the support. This is the general case for a large active primary mirror supported by a stiff structure, so the actuators are not coupled: If force f_i on actuator i changes, only the reaction forces on the hard points change. Forces do not change over the other actuators, because the axial mirror displacements over the soft springs, modeling the actuators, are very small. In the case of a (adaptive) mirror on the hard (piezoelectric) actuators, this is no longer true and all the actuators become coupled. Menikoff[10] described a method adapted to this kind of active mirror.

B. Pure Uniform Loading

We now consider a circular horizontal thin mirror with a central hole, under uniform loading and supported by a concentric ring of k discrete supports, with k-fold symmetry. Each support applies the same force, P/k, on the mirror rear surface. Load q is now given by

$$q = \frac{-P}{\pi(a^2 - c^2)} + \frac{P}{k}\frac{\delta(r - b)}{b}\sum_{j=1}^{k} \delta\left(\theta - \frac{2j\pi}{k} - \theta_0\right), \tag{32}$$

where θ_0 is the azimuth of the supports with respect to the origin axis. The term

$$\sum_{j=1}^{k} \delta\left(\theta - \frac{2j\pi}{k} - \theta_0\right)$$

can be written as a complex Fourier series:

$$\sum_{j=1}^{k} \delta\left(\theta - \frac{2j\pi}{k} - \theta_0\right) = \sum_{m=-\infty}^{\infty} c_m \exp(ikm\theta) \tag{33}$$

with

$$\begin{aligned} c_m &= \frac{1}{2\pi}\sum_{j=1}^{k}\int_0^{2\pi} \delta\left(\theta - \frac{2j\pi}{k} - \theta_0\right)\exp(-ikm\theta)\,d\theta \\ &= \frac{k}{2\pi}\exp(-ikm\theta_0). \end{aligned} \tag{34}$$

Therefore the load can be rewritten

$$\begin{aligned} q = \frac{-P}{\pi(a^2 - c^2)} + \frac{P\delta(r - b)}{2\pi b} + \frac{P\delta(r - b)}{\pi b} \\ \times \sum_{m=1}^{\infty} \cos[km(\theta - \theta_0)], \end{aligned} \tag{35}$$

where the deflection written as

$$w = w_0 + \sum_{m=1}^{\infty} w_m \cos[km(\theta - \theta_0)] \tag{36}$$

is assumed. The first two terms in Eq. (35) represent the load of a mirror supported by a continuous ring of radius b. The exact expressions of the associated ULIF or GIF w_0 can be computed from Ref. 6 or 7, respectively. Let us now consider the third term in Eq. (35) for which $m \geq 1$. Because $n = km > 1$, deflection w_m is given by

$$w_m = A_m r^n + B_m r^{n+2} + C_m r^{-n} + D_m{}^{-n+2}. \tag{37}$$

The ring of supports divides the mirror into two annular surfaces. Eight constants must be determined: $A_m', \ldots, D_m'$ for the inner annular surface and $A_m, \ldots, D_m$ for the outer annular surface. These constants are derived from a set of eight linear equations: Eqs. (6) and (7) for $r = a$ and $r = c$ and Eqs. (12)–(15). The expressions are

$$A_m - A_m' = \alpha = \frac{-b^{-n}}{n(n-1)} Q, \tag{38}$$

$$B_m - B_m' = \beta = \frac{b^{-n-2}}{n(n+1)} Q, \tag{39}$$

$$C_m - C_m' = \gamma = \frac{-b^{n}}{n(n+1)} Q, \tag{40}$$

$$D_m - D_m' = \delta = \frac{b^{n-2}}{n(n-1)} Q, \tag{41}$$

where

$$Q = \frac{Pb^2}{8\pi D} \tag{42}$$

and

$$A_m' = \frac{\lambda(3+\nu)(\nu-1)n(n+1)(1-\rho_0{}^{2n}) - \mu\kappa(1-\rho_0{}^{2n+2})a^2}{na^{2n}[-(3+\nu)^2(1-\rho_0{}^{2n})^2 + \mu(\rho_0{}^{n-1} - \rho_0{}^{n+1})^2]}, \tag{43}$$

$$B_m' = \frac{(\nu-1)[\lambda(3+\nu)n(1-\rho_0{}^{2n-2})a^{-2} - \kappa(n-1)(\nu-1)(1-\rho_0{}^{2n})]}{a^{2n}[(3+\nu)^2(1-\rho_0{}^{2n})^2 - \mu(\rho_0{}^{n-1} - \rho_0{}^{n+1})^2]}, \tag{44}$$

$$C_m' = \frac{(n-1)(\nu-1)}{3+\nu} c^{2n} A_m' + \frac{\mu}{n(3+\nu)(\nu-1)} c^{2n+2} B_m', \tag{45}$$

$$D_m' = n\frac{1-\nu}{3+\nu} c^{2n-2} A_m' + \frac{(1-\nu)(n+1)}{3+\nu} c^{2n} B_m', \tag{46}$$

where

$$\kappa = \frac{3+\nu}{1-\nu}\delta - na^{2n-2}\alpha - (n+1)\alpha^{2n}\beta, \tag{47}$$

$$\lambda = \frac{(n-1)(1-\nu)}{3+\nu} a^{2n}\alpha + \frac{\mu}{(3+\nu)(1-\nu)n} a^{2n+2}\beta + \gamma, \tag{48}$$

and finally

$$\mu = n^2(1-\nu)^2 + 8(1+\nu). \tag{49}$$

Deflection w [Eq. (36)] is now described fully. Note that when $b = 0$ the expressions for α, β, γ, and δ are undefined as is the solution for w. But the limit $w(b \to 0^+)$ smoothly converges toward the deflection of a plate supported by a central point (or a plate hanging at a wire attached at its center). Constants C_m' and D_m' cancel for $c = 0$, and the inner annular surface is therefore determined completely by A_m' and B_m', as in Ref. 4. When the series is programmed on a computer, it has been observed that the calculation of A_m by the direct addition of the numerical values of A_m' and α in Eq. (38) makes the series diverge because of the round-off errors for $n > \sim 30$, even in double precision, except in the case of a large (and thus unusual) central hole. The series also diverges when B_m is obtained with $B_m = B_m' + \beta$ [Eq. (39)]. To avoid numerical instabilities, the use of expressions for A_m and B_m versus α, β, γ, δ derived from Eqs. (38)–(49) is recommended, i.e.,

$$\begin{aligned} A_m \times d_a = {} & \alpha n c^{2n}[\mu(\rho_0{}^{-2} - 1) - (3+\nu)^2(\rho_0{}^{2n} - 1)] \\ & + \beta\mu(n+1)c^{2n+2}(1 - \rho_0{}^{-2}) \\ & - \gamma(3+\nu)(1-\nu)n(n+1)(1-\rho_0{}^{2n}) \\ & - \delta\mu\frac{3+\nu}{1-\nu}(1-\rho_0{}^{2n+2})a^2, \end{aligned} \tag{50}$$

where

$$\begin{aligned} d_a = {} & na^{2n}[-(3+\nu)^2(1-\rho_0{}^{2n})^2 \\ & + \mu(\rho_0{}^{n-1} - \rho_0{}^{n+1})^2], \end{aligned} \tag{51}$$

$$\begin{aligned} B_m \times d_b = {} & \alpha n(1-\nu)^2(n-1)c^{2n-2}(1-\rho_0{}^{-2}) \\ & + \beta c^{2n}[\mu(1-\rho_0{}^2) + (3+\nu)^2(\rho_0{}^{2n} - 1)] \\ & - \gamma(3+\nu)(1-\nu)n(1-\rho_0{}^{2n-2})a^{-2} \\ & - \delta(1-\nu)(3+\nu)(n-1)(1-\rho_0{}^{2n}), \end{aligned} \tag{52}$$

where

$$d_b = -\frac{d_a}{n}. \tag{53}$$

5. Support Pads of Finite Size

As pointed out in Section 3, and assumed in Section 4, the size of the support pads was neglected in the expression of q [Eq. (2), (3), or (32)]. This leads to a value for the deformation that is too large: A finite pad spreads the load under the mirror and smooths the shape of the optical surface. Most of the time the support pads are circular, but here, for mathematical convenience, and probably without changing the final result significantly, the pads considered are almost squares of dimension d_p and defined by the product

$$\Pi\left[\frac{(r - b_j)}{d_p}\right] \times \Pi\left[\frac{b(\theta - \theta_j)}{d_p}\right], \tag{54}$$

where

$$\Pi[x] = 1, \quad x < 0.5, \qquad \Pi[x] = 0, \quad x \geq 0.5. \tag{55}$$

Therefore the general expression of the load q can be written as

$$q = \frac{-P}{\pi(a^2 - c^2)} + \sum_{j=1}^{k} \frac{f_j}{{d_p}^2}\, \Pi\left[\frac{(r - b_j)}{d_p}\right] \times \Pi\left[\frac{b(\theta - \theta_j)}{d_p}\right] \tag{56}$$

or

$$q = \frac{-P}{\pi(a^2 - c^2)} + \sum_{j=1}^{k} \frac{f_j}{2\pi b_j d_p}\, \Pi\left[\frac{(r - b_j)}{d_p}\right] \times \sum_{m=-\infty}^{\infty} \operatorname{sinc}\left(\frac{m d_p}{2\pi b_j}\right) \exp[im(\theta - \theta_j)] \tag{57}$$

if $\Pi[b(\theta - \theta_j)/d_p]$ is replaced by its Fourier series. The deflection associated with the harmonic $m = 0$ corresponds to the case of a continuous ring of width d_p. This deflection can easily be calculated by the solutions in Ref. 6 or 7 and by applying Saint-Venant's principle,[2] which states that if a system of forces acting on a small portion of the surface of an elastic body is replaced by a statically equivalent system of forces acting on the same portion of surface, the variation in the displacements in parts of the body that are at great distance compared with the linear dimensions of the surface on which the forces are changed are negligible. Therefore the superposition of deflections calculated from Ref. 6 or 7 for different equidistant rings between $b_j - d_p/2$ and $b_j + d_p/2$, with each carrying a fraction of the weight proportionally to its radius, gives an accurate estimation of the deflection for $m = 0$. For harmonic $m > 0$ the uniform Fourier spectrum obtained in Sections 3 and 4 for the Dirac function $\delta(\theta - \theta_j)$ is now multiplied by the function $\operatorname{sinc}(x) = \sin(\pi x)/\pi x$. Thus a good estimation of w_m is obtained simply by multiplying the w_m expressions from Sections 3 and 4 by $\operatorname{sinc}(m d_p/2\pi b_j)$. The effect of pads of finite size is illustrated in Fig. 4 showing the radial deformation of the ESO NTT primary mirror along a radius with four actuators, each with a square pad of 50 mm × 50 mm. The peak-to-valley (ptv) surface error is noticeably reduced in the vicinity of the pads, but the rms remains almost the same.

6. Application to the Optimization of Active Mirror Supports

A. Overview

Optimizing a mirror support classically consists of minimizing the variance ${w_{\text{rms}}}^2$ of the deflection w caused by gravitational loading:

$${w_{\text{rms}}}^2 = \iint_{\text{pupil}} (w + p_0)^2 \mathrm{d}S = \iint_{\text{pupil}} \left[\sum_{i=1}^{I} \eta_i w_i + p_0\right]^2 \mathrm{d}S \tag{58}$$

or

$${w_{\text{rms}}}^2 = \iint_{\text{pupil}} \left[\sum_{i=1}^{I} \eta_i w_i + p_0 + p_2\rho^2\right]^2 \mathrm{d}S, \tag{59}$$

where $\mathrm{d}S = \rho \mathrm{d}\rho \mathrm{d}\theta$ is the pupil's infinitesimal surface element where ρ is the normalized radius r/a and θ is the azimuth over the pupil. Deflection w is the superposition of deflections w_i, where η_i represents a fraction of the load supported by a set of points i. This type of optimization has been done before, for example, for the ESO NTT 3.6-m telescope. Note that the rms of the slopes $(\nabla w)_{\text{rms}}$ is also relevant for the image degradation in the atmosphere,[11] so a trade-off between the minimization of ${w_{\text{rms}}}^2$ and ${(\nabla w)_{\text{rms}}}^2$ could be found. In such a calculation one should consider simply the minimization of the image size.

Term p_0 is a piston term. Eq. (59) applies only if a small parabolic deformation $p_2\rho^2$ is tolerated on the mirror. Note that this deformation decreases slowly when the telescope moves from zenith to horizon, thus producing a small change in focal length. Several sets of support topologies are discussed in Refs. 4 and 14. Although the idea of servoing telescope collimation, focusing, or even mirror deformation corrections appeared in the 1960's,[15] the active-optics concept was finally developed in the 1980's by Wilson and co-workers[16–19] at ESO. The ESO NTT is the first large telescope implementing this technique. Nevertheless its 3.6-m mirror support topology was calculated according to Eq. (58) to minimize the rms of the GIF, as would have been done for a passive support.

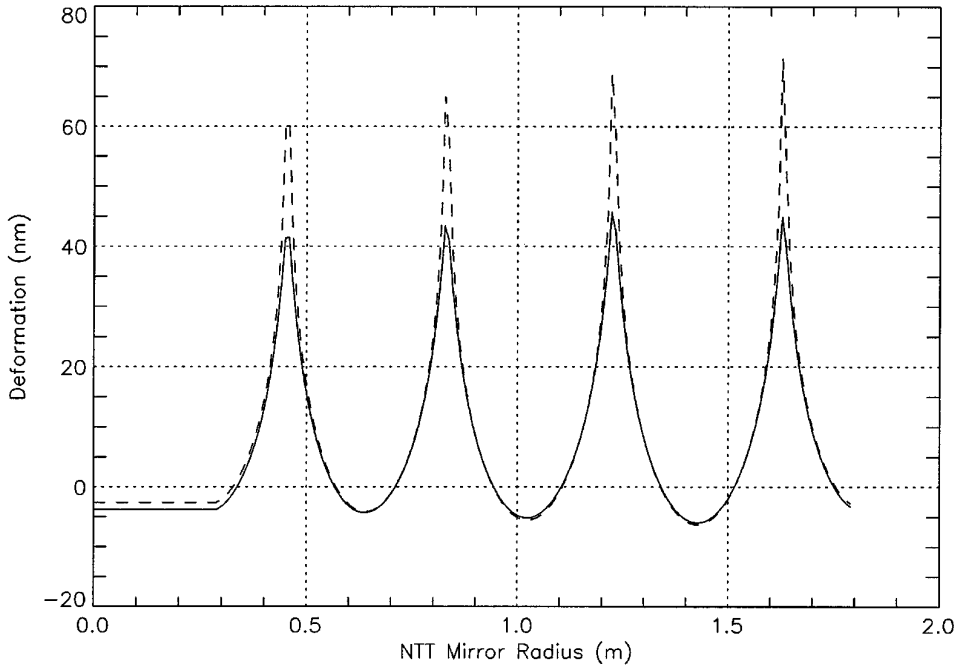

Fig. 4. Deformation of the ESO NTT primary mirror along a radius with four supports. The dashed curve represents the deformation for supports of neglected size. The surface error is 81 nm ptv and 8.8 nm rms. The solid curve represents the deformation for roughly square supports of 50 mm × 50 mm. The surface error is reduced to 56 nm ptv but is still 8.3 nm rms. In the two cases the calculation takes into account an estimation of the noticeable effect of shear forces because of the 241-mm thickness.

I now show that the active-support correction range can be enlarged by taking into account not only the minimization of the GIF but also the optimization of the correction of low-order aberrations, such as third-order astigmatism. These aberrations typically come from polishing errors in the case of relaxed polishing specifications, collimation failures, telescope flexures, support failures, thermal gradients, or wind buffeting.

The larger the correction range, the more the polishing specifications can be relaxed for low-spatial-frequency errors, thus leading to additional cost reduction.

A change in the mirror shape may also be required when one switches from the Cassegrain to the Nasmyth configuration,[20] demanding adequate performance from the actuators and thus a particular arrangement of the actuators in the active mirror cell.

B. Optimization Method

If the optimization of the AIF to fit a given set of modes, i.e., low-order aberrations, is integrated into the active-mirror support calculation, the variance ${w_{\mathrm{rms}}}^2$ for minimizing can be written

$$ {w_{\mathrm{rms}}}^2 = \iint_{\mathrm{pupil}} \left[\sum_{i=1}^{I} \eta_i w_i + p_0'' + p_2''\rho^2 + \sum_{n,m} \left(\sum_{j \geq 1}^{J \leq I} F_j w_{m,j} - a_{nm} {Z_n}^m + p_{0nm}'' + p_{2nm}''\rho^2 \right) \right]^2 \mathrm{d}S. \tag{60} $$

Terms p_2'' or p_{2nm}'' are zero if no parabolic deformation is tolerated on the mirror. The sum over n and m represents the set of aberrations (modes) to be fitted. The maximum number of controllable orthogonal modes that can be considered in the optimization is fixed by support topology: Assuming that the actuators are on a set of I different rings, the maximum number of controllable radial orthogonal modes is I for cases in which $m > 1$ and $I - 1$ for cases $m = 0, m = 1$.

Aberrations are described in Eq. (60) over the Zernike modes ${Z_n}^m$,[21–24] weighted by their amplitude a_{nm}.

Noethe[25] showed that aberrations from the optical origin (polishing errors or collimation) are better described by the Zernike modes and that the aberrations of elastic origin are better described by the minimum energy modes. In the case of wave-front distortions induced by atmospheric turbulence, Karhunen–Loève modes should be used.[26] Other aberration expansions are yet to be considered.[16,27] It is also important that the wave-front sensor be optimized for the detection of each mode.

The $w_{m,j}$ term is a mirror deformation with m-fold symmetry, as is ${Z_n}^m$, obtained by a cosinusoidal distribution of forces f_{js} on ring j. Force f_{js} on the sth actuator from ring j is

$$ f_{js} = \cos\left[2\pi m \frac{(s-1)}{S} + \theta_j \right], \tag{61} $$

where $s = 1, \ldots, S$ and θ_j represents a reference azimuth on the mirror. The cosinusoidal distribu-

tion of forces is convenient because it involves only one free parameter per ring of actuators, namely, F_j. But it is clear that forces f_{js} could be computed separately, leading to a greater number of free parameters, which is nevertheless constrained by the azimuthal symmetry m of the desired deformation. This would be lengthy to compute for probably only a small improvement in the fitting. If $w_{m,j}$ contains no piston term, p_{0nm} can be set to zero. If w_i and $w_{m,j}$ do not have the same rotational symmetry, they are orthogonal functions and the variance becomes, when the coefficients of the parabolic deformation are renamed,

$$w_{\mathrm{rms}}{}^2 = \iint_{\mathrm{pupil}} \left[\left(\sum_{i=1}^{I} \eta_i w_i \right)^2 + (p_0{}' + p_2{}' \rho^2)^2 + \sum_{n,m} \left(\sum_{j \geq 1}^{J \leq I} F_j w_{m,j} - a_{nm} Z_n{}^m \right)^2 \right] \mathrm{d}S, \tag{62}$$

which can be rewritten by again renaming the coefficients of the parabolic deformation:

$$w_{\mathrm{rms}}{}^2 = \iint_{\mathrm{pupil}} \left(\sum_{i=1}^{I} \eta_i w_i + p_0 + p_2 \rho^2 \right)^2 \mathrm{d}S + \sum_{n,m} \iint_{\mathrm{pupil}} \left(\sum_{j \geq 1}^{J \leq I} F_j w_{m,j} - a_{nm} Z_n{}^m + p_{0nm} + p_{2nm} \rho^2 \right)^2 \mathrm{d}S. \tag{63}$$

Minimizing $w_{\mathrm{rms}}{}^2$ is a delicate task, because it involves minimization in a space of dimension I, which can be noticeably larger than $I = 1$. A downhill simplex algorithm is used to find the best support topology (radii b_i and azimuth θ_i) coupled with a least-squares method[7,14,28] to calculate η_i and F_j for each set of positions chosen by the simplex. These topologies are verified by simulated annealing with a slow temperature decrease.[14,28] Note that even with slow annealing, one cannot be sure to have found the global minimum and the best support topology. In any case the local minima values are close to the global minimum one, assuming that it has been found. The support topology has been sought for a mirror-surface sampling of 19,872 points (288×69, for the angular and radial directions, respectively). The Fourier series was truncated after 16 terms for the GIF and 11 for the AIF. These truncations do not affect the computed rms deformation by more than $\sim 0.1\%$ and permit computing time to be saved.

C. Results and Discussion

To illustrate the method, we consider the case of the ESO NTT (Table 1) and the correction of pure third-order astigmatism of optical origin. Third-order astigmatism, Zernike mode $Z_2{}^2$, would have been induced on the mirror if polishing specifications had been relaxed. Here we assume the presence of $Z_2{}^2$, which also represents the main contribution to the wave-front error of common mirror deformations. This mode is defined here by

$$Z_2{}^2 = \rho^2 \cos(2\theta + \theta_{22}). \tag{64}$$

The azimuthal origin θ_{22} is chosen to equal zero. Terms p_2, $p_{0,nm}$, and p_{0nm} in Eq. (63) are at zero. A correction based on the two external rings of actuators is assumed, as proposed by Schwesinger.[7] Schwesinger also determined that the deformation of the optical surface had to be reduced by a factor of ~ 1.90, because the shear effects computed with the GIF give the average deformation across the thickness and do not take into account the spreading of the shear effects from supports to optical surface. With this assumption, and by taking into account the finite size of the support pads, a wave-front error over the entire mirror surface of 58 nm ptv and 9 nm rms is found for the current NTT support and an aberration-free mirror, when the ULIF is used with the shear effect included. This is in good agreement with FEA calculations[7] of 56 nm ptv, which shows that the ULIF can be used as a good approximation of the GIF. Only a small parabolic deformation w is observed [$w \sim -32(r/a)^2$ nm on the glass] when the four-continuous-ring configuration minimizing the GIF is used to compute the ULIF. One can easily balance this deformation by readjusting the weight carried by each ring of support. Further verification of the ULIF has been made by setting $c = 0$. The series from Subsection 4.B., computed for a thin mirror, thus becomes equivalent to that of Nelson *et al.*[4] Truncating these two series after an equal number of terms gives exactly the same results, which confirms the correctness of the ULIF given in Subsection 4.B. To verify the AIF of Subsection 4.A., the forces needed to produce pure astigmatism on the primary were calibrated; the ULIF was neglected for this calculation. Force values are 4% larger than those computed by Schwesinger. The difference is probably a result of this author using a more exact theory than Wan's approximation for the computation of the shear effects. The mean rms residual errors represent $\pm 0.4\%$ of the target deformation, as found by Schwesinger.

The numerical results of the minimization of $w_{\mathrm{rms}}{}^2$ are in Figs. 5–7. Figure 5 shows the computed decrease d of the residual error after correction by the actuators of a given amount a_{22} for which active support has been optimized with respect to a residual error obtained with the current support: The decrease is $\sim 35\%$ for an initial astigmatic amplitude error of $a_{22} = 5\lambda = 2800$ nm. The corresponding multiplicative factor MF of the current correction range can be written as

$$MF = \frac{1}{1 - d}, \tag{65}$$

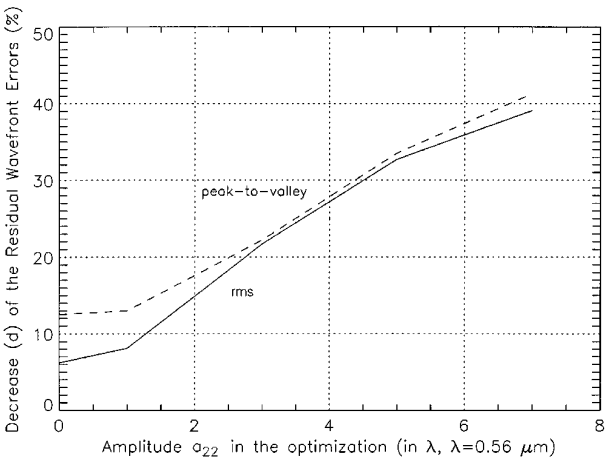

Fig. 5. NTT primary-mirror active support: computed decrease d of the residual wave-front error obtained with optimized active supports with respect to the residual wave-front error obtained by the current ESO NTT active support. The topologies are optimized only over the clear aperture, from the internal stop to the outer edge. The improvement in the wave front is calculated with respect to the performances measured over the same clear aperture for the current support.

and its value is ~1.5 for the support optimized for $a_{22} = 5\lambda = 2800$ nm (Fig. 6).

Figures 7A and 7C show the very similar wave-front errors of the aberration-free mirror supported by the two optimized supports. Figure 7B shows that the maximum error, after the astigmatism is corrected, occurs currently at the mirror edge: High-order bending modes of azimuthal symmetry, $m = 2$, are excited by the actuators. They can be practically balanced by an adequate support topology (Fig. 7C). Optimization has been performed to $a_{22} = 7\lambda = 3920$ nm, but for this value calculations showed that the external supports had to be placed exactly at the mirror edge, which is not reasonable from a mechanical point of view. Thus it was assumed that $a_{22} = 5\lambda = 2800$ nm was the maximum value for which the

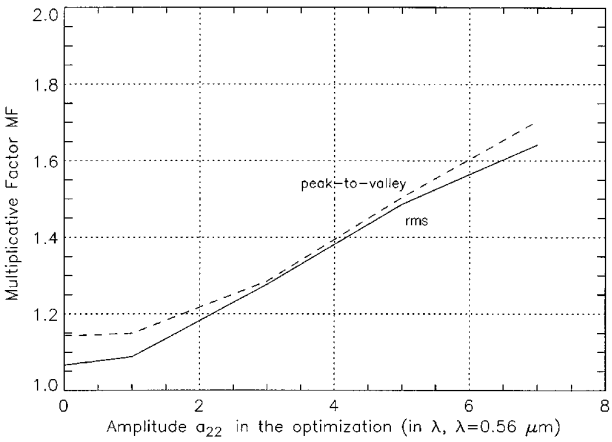

Fig. 6. NTT primary-mirror active support: expected multiplicative factor *MF* applied to the correction range from the current ESO NTT active support for the case of astigmatic correction.

support could be optimized. The final results are in Table 2. It can be seen that the support radii are all larger for the topology optimized for $a_{22} = 5\lambda = 2800$ nm than for the classic support because the actuators must be placed at the mirror's edge to produce the best radial bending moment and thus the best parabolic meridian for astigmatism. A result of this displacement is that the passive weight carried by the third ring becomes higher for the topology optimized for $a_{22} = 5\lambda = 2800$ nm than for classic support, which requires a rigid mirror cell because the third ring carries ~38% of the mirror weight. On the other hand, the calibrated forces F_j become smaller.

To test the robustness of the method, I studied the modification of the correction capability of the third-order spherical aberration, proportional to ρ^4 (an approximate Zernike Z_4^0), for supports designed for an optimal Z_2^2 correction. Results are encouraging because improvement for Z_4^0 is of the same order as for Z_2^2 ($nf \sim 1.7$).

Nevertheless, if Z_4^0 compensation can tolerate a extra defocusing, better results are obtained for the topology optimized with $a_{22} = 0\lambda$: If defocusing is tolerated, the generated deformation is close to the first elastic mode with $m = 0$ where the curvature at the outer edge is close to zero.[29] This deformation is then better balanced if the outer ring of support is farther from the outer edge. Note that the correction is excellent for the two topologies tolerating defocus and optimized with $a_{22} = 0\lambda$ and $a_{22} = 5\lambda$, and the wave-front residual rms error is less than 0.63% of the target deformation. Table 2 shows wave-front errors after active correction of third-order spherical aberration, $\lambda\rho_4 = 560\ \rho^4$ nm, on the glass for two methods of spherical aberration compensation. The first method does not tolerate extra defocusing; the second one does. The value of parameter p_2 [Eq. (60)] is then approximately -2.5 μm, leading to a variation δF in the primary-mirror focal length F:

$$\delta F = 16\left(\frac{F}{2a}\right)^2 p_2 \sim -200\ \mu\text{m}. \tag{66}$$

Finally, note that the results are even better if the ULIF is noticeably smaller than the residual errors of an active correction. If the ULIF is neglected, only the fit of the polynomials Z_n^m by the combined AIF's is optimized. This is the case in the design of a small, lightweight adaptive mirror, for which gravity effects are negligible and for which the actuators' locations must be especially optimized to allow the best correction of the input distorted wave front. It can be shown that for atmospheric distortion correction, Karhunen–Loève functions are more efficient than Zernike modes.[26,30] Each mode is then weighted by a_{nm} computed from the parameter of atmospheric turbulence[31] $2a/r_0$. The optimization procedure should also take into account the actual size of the actuators to avoid their overlap when a circumferential radial bending moment is needed.

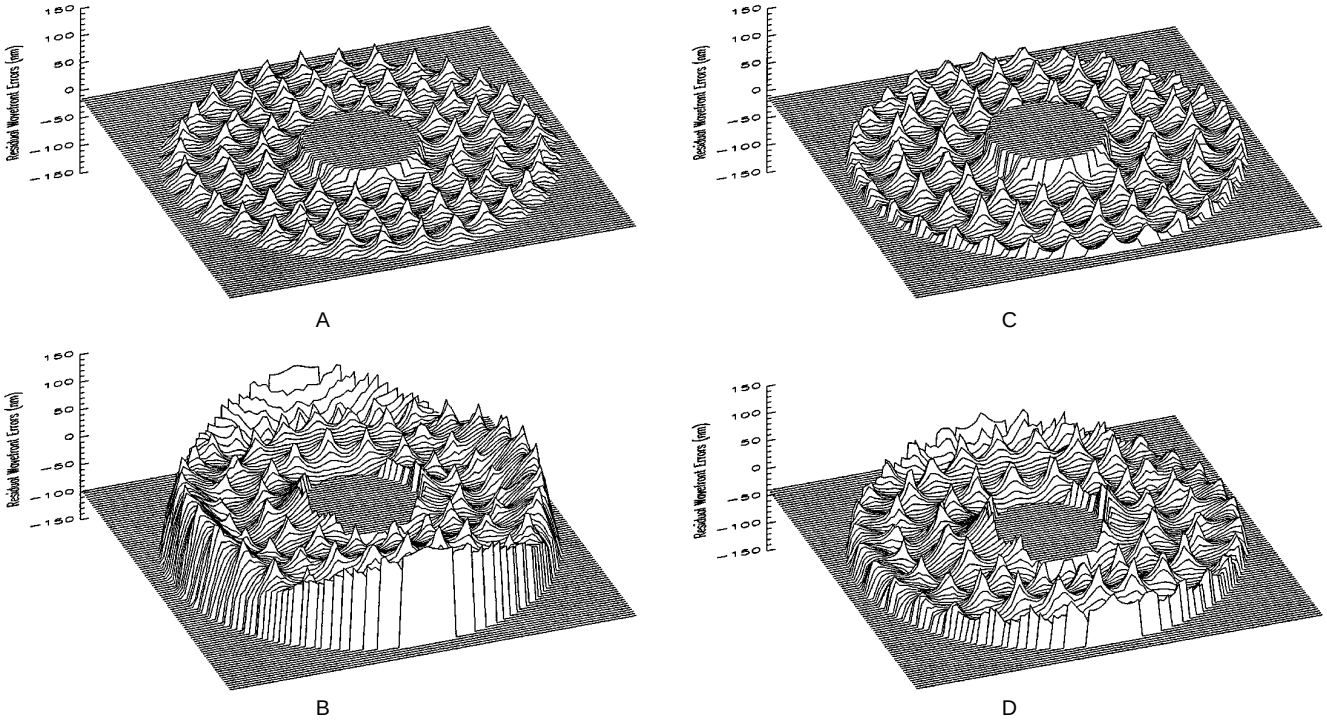

Fig. 7. Three-dimensional views of the mirror deflection: A, deflection calculated for the current support design, representing the pure ULIF for an aberration-free mirror. B, deflection calculated for the same support as A, representing the mirror after the active supports have compensated for pure third-order astigmatism, $5\lambda\rho^2\cos(2\theta) = 2800\rho^2\cos(2\theta)$ nm, on the glass. It can be seen that high-order bending modes of azimuthal symmetry, $m = 2$, are excited by the actuators. C, deflection calculated for an optimized active support design, representing the pure ULIF for an aberration-free mirror. The mirror support was calculated so that a large amount of pure third-order astigmatism, $5\lambda\rho^2\cos(2\theta) = 2800\rho^2\cos(2\theta)$ nm, on the glass could be corrected. D, deflection calculated for the same optimized support as for C, representing the mirror after the active supports have compensated the pure third-order astigmatism integrated in the active support optimization. High-order bending modes are now practically absent. Note that the effects of the small bumps on the inner supports are not visible because they are in the shadow of the aperture stop. Peak-to-valley and rms errors for each figure are in Table 2.

Table 2. NTT Primary Support: Topologies for an Optimized Active Support Design[a]

Content	Topology Optimized for $a_{22} = 0\lambda$	Topology Optimized for $a_{22} = 5\lambda = 2800$ nm
Ring i =	b_i(m), η_i	b_i(m), η_i
1 (inner)	0.4997, 0.13439	0.5219, 0.15317
2	0.8959, 0.20498	0.9668, 0.25701
3	1.2576, 0.29508	1.3818, 0.37671
4 (outer)	1.6371, 0.36555	1.7453, 0.21312
Wave-front errors		
For $a_{nm} = 0$	53 nm ptv, 8 nm rms	66 nm ptv, 10 nm rms
After correction of $a_{22} = 5\lambda = 2800$ nm	174 nm ptv, 21 nm rms	126 nm ptv, 15 nm rms
After correction of $a_{22} = 7\lambda = 3920$ nm	240 nm ptv, 28 nm rms	159 nm ptv, 19 nm rms
After correction of $a_{40} = \lambda = 560$ nm and GIF neglected:		
With Z_2^0 not tolerated	99 nm ptv, 21 nm rms	60 nm ptv, 12 nm rms
With Z_2^0 tolerated	11 nm ptv, 1.5 nm rms	21 nm ptv, 3.5 nm rms
If Z_2^0 is tolerated [Eq. (60)]	$p_{222} = -2416$ nm	$p_{222} = -3231$ nm
Forces for $a_{22} = \lambda = 560$ nm	$F_3 = -48.83$ N, $F_4 = 49.60$ N	$F_3 = -44.12$ N, $F_4 = 46.22$ N

[a]The optimization considers only the clear aperture, from internal stop to outer edge, and not the whole mirror surface, from inner hole to outer edge. Thus the topology for $a_{22} = 0$ is different and slightly better than that in Ref. 7. The amplitude a_{22} is defined with respect to astigmatism $a_{22}\rho^2\cos(2\theta)$ on the glass. The variable η_i represents the fraction of weight supported by the ring i of radius b_i. The robustness of the proposed topologies has been tested by simulated annealing for the mirror surface sampling cited in the text.

7. Conclusion

The numerical results derived from the ULIF and AIF Fourier series for a mirror with a central hole and uniform thickness are in good agreement with the previously published FEA results carried out for the ESO NTT.[7] Therefore we can use the results in Sections 3 and 4 for designing either passive or active mirror supports, following the method described in Section 6. It was shown that large active mirror supports should be designed not only by minimizing the rms of the ULIF or the GIF, as is commonly done, but also by optimizing combinations of AIF's to fit common mirror aberrations. This allows a relaxation of soft polishing specifications for cost reduction. In the example studied here, it is shown that the residual errors can be reduced, leading to expected improvements in the correction range by a multiplicative factor to ~ 1.5.

Finally, the following design of an active support is recommended: According to the total number of actuators and their location under the mirror, a maximum number of controllable orthogonal modes is defined. Large polishing errors of low spatial frequency should be introduced into this set of modes. The actuator locations and forces are then adjusted to minimize both the variance of the deflection from modes excited by gravitational loading and the variance of the high-spatial-frequency residual errors after the correction of each mode, i.e., the high-order modes excited by the actuators after a correction.

This research was supported by the Laboratoire d'Astrophysique Observationnelle, Collège de France, Paris. Constructive comments on a preliminary version of the manuscript by L. Koechlin, L. Noethe, G. Schwesinger, D. S. Wang, and the two referees are gratefully acknowledged. The author also thanks P. Lawson and D. Mourard from the G12T team, Observatoire de la Côte d'Azur, for carefully reading the manuscript and G. Schumacher for an introduction to MAPLE V software.

References

1. A. Couder, "Recherches sur les déformations des grands miroirs employés aux observations astronomiques," Thesis (Gauthier-Villars et C^ie, Paris, 1932).
2. A. E. H. Love, *A Treatise on the Mathematical Theory of Elasticity* (Dover, New York, 1944).
3. S. Timoshenko and S. Woinowsky-Krieger, *Theory of Plates and Shells* (McGraw-Hill, New York, 1959), Chap. 9.
4. J. E. Nelson, J. Lubliner, and T. S. Mast, "Telescope mirror supports: plate deflection on point supports," in *Advanced Technology Optical Telescopes I*, L. D. Barr and G. Burbridge, eds., Proc. Soc. Photo-Opt. Instrum. Eng. **332,** 212–228 (1982).
5. G. Schwesinger and E. D. Knohl, "Comments on a series of articles by L. A. Selke," Appl. Opt. **11,** 200–202 (1972).
6. L. A. Selke, "Theoretical elastic deformations of solid and cored horizontal circular mirrors having a central hole on a ring support," Appl. Opt. **10,** 939–944 (1971).
7. G. Schwesinger, "An analytical determination of the flexure of the 3.5 m primary and 1 m mirror of the ESO's New Technology Telescope for passive support and active control," J. Mod. Opt. **35,** 1117–1149 (1988).
8. G. Schwesinger, "Support configuration and elastic deformation of the 1.5 m prime mirror of the ESO Coudé Auxiliary Telescope (CAT)," ESO Tech. Rep. 9 (European Southern Observatory, Garching-bei-München, Germany, 1979).
9. D. S. Wan, J. R. P. Angel, and R. E. Parks, "Mirror deflection on multiple axial supports," Appl. Opt. **28,** 354–362 (1989).
10. A. Menikoff, "Actuator influence function of active mirrors," Appl. Opt. **30,** 833–838 (1991).
11. P. Dierickx, "Optical performance of large ground-based telescopes," J. Mod. Opt. **39,** 569–588 (1992).
12. A. J. Ostroff, "Evaluation of control laws and actuators locations for control systems applicable to deformable astronomical telescope mirrors," NASA Tech. Note D-7276 (Oct. 1973).
13. F. B. Ray and Y. T. Chung, "Surface analysis of an active controlled telescope primary mirror under static loads," Appl. Opt. **24,** 564–569 (1985).
14. L. Arnold, "Optimized axial support topologies for thin telescope mirrors," Opt. Eng. **34,** 567–574 (1995).
15. B. Rule, "Possible flexible mirror and collimation servo-control," in *The Construction of Large Telescopes*, D. L. Crawford, eds., IAU Symposium 27 (Academic, London, 1966), pp. 71–75.
16. R. N. Wilson, F. Franza, and L. Noethe, "Active optics I: A system for optimizing the optical quality and reducing the costs of large telescopes," J. Mod. Opt. **34,** 485–509 (1987).
17. L. Noethe, F. Franza, P. Giordano, and R. N. Wilson, "Active optics II: Results of an experiment with a thin 1 m test mirror," J. Mod. Opt. **35,** 1427–1457 (1988).
18. R. N. Wilson, F. Franza, P. Giordano, L. Noethe, and M. Tarenghi, "Active optics III: Final results with the 1 m test mirror and the NTT 3.58 m primary in the workshop," J. Mod. Opt. **36,** 1415–1425 (1989).
19. R. N. Wilson, F. Franza, L. Noethe, and G. Andreoni, "Active optics IV: Setup and performance of the optics of the ESO New Technology Telescope (NTT) in the observatory," J. Mod. Opt. **38,** 219–243 (1991).
20. D. Enard, B. Delabre, S. D'Odorico, F. Merkle, A. Moorwood, G. Raffi, M. Sarazin, M. Schneermann, J. Wampler, R. Wilson, L. Zago, and M. Ziebell, "Proposed for the construction of the 16-m Very Large Telescope" (European Southern Observatory, Garching-bei-München, Germany, 1987).
21. M. Born and E. Wolf, *Principles of Optics* (Pergamon, New York, 1975).
22. V. N. Mahajan, "Zernike annular polynomials for imaging systems with annular pupils," J. Opt. Soc. Am. **71,** 75–85 (1981).
23. V. N. Mahajan, "Zernike annular polynomials for imaging systems with annular pupils: errata," J. Opt. Soc. Am. **71,** 1408 (1981).
24. V. N. Mahajan, "Zernike annular polynomials for imaging systems with annular pupils," J. Opt. Soc. Am. A **1,** 685 (1984).
25. L. Noethe, "Use of minimum-energy modes for modal-active optics corrctions of thin meniscus mirrors," J. Mod. Opt. **38,** 1043–1066 (1991).
26. J. Y. Wang and J. K. Markey, "Modal compensation of atmospheric turbulence phase distortion," J. Opt. Soc. Am. **68,** 78–87 (1978).
27. B. Tatian, "Aberration balancing in rotationally symmetric lenses," J. Opt. Soc. Am. **64,** 1083–1091 (1974).
28. W. H. Press, S. A. Teukolsky, W. T. Vettering, and B. P. Flannery, *Numerical Recipies in C* (Cambridge U. Press, 1992).
29. L. Noethe, European Southern Observatory, Karl Schwarzschild, Strasse 2, D-W 8046, Garching-bei-München, Germany (personal communication, 1995).
30. F. Roddier, "The problematic of adaptive optics design," in *Adaptive Optics for Astronomy*, D. M. Alloin and J. M. Mariotti, eds. (Kluwer Academic, Boston, Mass., 1994), Vol. 423, pp. 89–111.
31. R. J. Noll, "Zernike polynomials and atmospheric turbulence," J. Opt. Soc. Am. **66,** 207–211 (1976).